Institute of Physics Publishing Journal of Physics: Conference Series **16** (2005) 91–100
doi:10.1088/1742-6596/16/1/011 SciDAC 2005

Interaction of turbulence, chemistry, and radiation in strained nonpremixed flames

Chun Sang Yoo and Hong G. Im*

Department of Mechanical Engineering
University of Michigan, Ann Arbor, MI 48109-2125

Yi Wang and Arnaud Trouvé

Department of Fire Protection Engineering
University of Maryland, College Park, MD20742-3031

*Corresponding author: hgim@umich.edu

Abstract. This paper provides an overview of recent progress in our development of high-fidelity simulation of turbulent combustion with detailed chemistry. In particular, two major accomplishments are presented and discussed: (a) As for the computational aspects, it was recognized that many existing techniques to treat inflow and outflow boundary conditions for compressible flow simulations suffered from spurious errors when applied to highly turbulent reacting flow problems. Upon careful examination, the sources of these problems have been identified and an improved characteristic boundary condition strategy has been developed. The new method has been applied to various test problems, thereby demonstrating that the improved boundary conditions can successfully reproduce complex combustion events in a finite domain size with desired accuracy and stability. (b) As a science application, more advanced physical models for soot formation and radiative heat transfer have been developed in order to provide fundamental understanding of the interaction among turbulence, chemistry and radiation. We have performed several parametric simulations of two-dimensional ethylene-air nonpremixed counterflow flames interacting with counter-rotating vortex pairs and injected turbulent flows to investigate transient dynamics of soot formation process. Detailed analysis on the transient characteristics of soot behavior is discussed.

1. Introduction

Recent advances in the parallel computing technology have enabled high-end direct numerical simulations (DNS) of laminar and turbulent reacting flows to unravel fine-scale physics with utmost realism and accuracy. To achieve this goal successfully, it is essential to develop reliable numerical algorithms that are robust, stable, and free from artificial dissipation. Furthermore, efficient implementation of advanced physical models is needed in order to allow quantitative investigation of many challenging issues arising from the complex interaction between turbulence, chemistry, and heat transfer. A multi-university collaboration [1] has thus launched to develop advanced high-fidelity simulation capability to investigate fundamental science relevant to turbulent combustion problems. The major tasks under this project involve implementation of advanced physical models, such as radiation, soot, and spray, into the structured-grid, high-order, non-dissipative reacting flow solver, thereby providing a computational diagnostic tool for spray dynamics, combustion, and pollutant

formation processes that can impact the development of high-performance, low-emission combustion devices.

This paper presents an overview of our recent accomplishments in this endeavor. In particular, two major advancements in numerical and physical aspects will be highlighted and discussed: (a) improved characteristic boundary conditions for compressible reacting flows, and (b) advanced radiation and soot formation submodels, and their application to the study of flame-vortex interaction.

Since high-fidelity DNS is often limited to a finite domain size due to the cost consideration, it is critical to provide a proper treatment of acoustic waves incident on the artificial boundaries. While this issue has been studied extensively [2-7] in the aeroacoustics community, and the approach has been applied to reacting flow simulations [8-11], researchers have encountered persisting problems with numerical instability and spurious acoustic wave reflections. Although some limited attempts were made to alleviate the problem of flame passing through the boundary [12], many such efforts were limited to specific problems, and a more general understanding of this subject was needed. We have recently revisited this issue and successfully derived improved boundary conditions that are applicable to general convective, viscous, reacting flows with minimal numerical artifacts [13,14]. A brief description of the theoretical basis and test examples will be discussed.

The latter part of the paper describes the radiation model and its application to the study of unsteady flow-flame interaction. While a number of papers exist on the numerical modeling of soot and radiation in steady flame configurations, few studies have explored the transient characteristics of the soot, radiation, and flame interaction in detail [15,16]. Employing an optically-thick gray-gas radiation and semi-empirical soot models, along with the improved characteristic boundary conditions, we have performed simulations of a counterflow sooting ethylene-air diffusion flame perturbed by strong vortices. The high-fidelity simulation data allow spatially and temporally resolved information of the flame-vortex interaction and its impact on the overall soot behavior. Comparison of results with different radiation models is also made, and significant findings on the soot formation in unsteady combustion processes are discussed.

2. Characteristic boundary conditions

The characteristic boundary conditions are based on a one-dimensional characteristic analysis of the different waves crossing a given boundary of the computational domain. The compressible Navier-Stokes equations for multi-component reacting flows in the characteristic form are written as [13,14]:

$$\frac{\partial}{\partial t}\begin{bmatrix} u \\ v \\ w \\ \rho \\ p \\ Y_i \end{bmatrix} + \begin{bmatrix} \left(L_5^{(x)} - L_1^{(x)}\right)/\rho c \\ L_3^{(x)} \\ L_4^{(x)} \\ L_2^{(x)} + \left(L_5^{(x)} + L_1^{(x)}\right)/c^2 \\ L_5^{(x)} + L_1^{(x)} \\ L_{5+i}^{(x)} \end{bmatrix} + \begin{bmatrix} \mathbf{v}_t \cdot \nabla_t u \\ \mathbf{v}_t \cdot \nabla_t v + (1/\rho)\partial p/\partial y \\ \mathbf{v}_t \cdot \nabla_t w + (1/\rho)\partial p/\partial z \\ \mathbf{v}_t \cdot \nabla_t \rho + \rho \nabla_t \cdot \mathbf{v}_t \\ \mathbf{v}_t \cdot \nabla_t p + \gamma p \nabla_t \cdot \mathbf{v}_t \\ \mathbf{v}_t \cdot \nabla_t Y_i \end{bmatrix} = \begin{bmatrix} d_u \\ d_v \\ d_w \\ d_\rho \\ d_p \\ d_{Y_i} \end{bmatrix} + \begin{bmatrix} s_u \\ s_v \\ s_w \\ s_\rho \\ s_p \\ s_{Y_i} \end{bmatrix}, \tag{1}$$

where

$$\begin{bmatrix} L_1^{(x)} \\ L_2^{(x)} \\ L_3^{(x)} \\ L_4^{(x)} \\ L_5^{(x)} \\ L_{5+i}^{(x)} \end{bmatrix} = \begin{bmatrix} (u-c)/2 \cdot (\partial p/\partial x - \rho c\, \partial u/\partial x) \\ u\left(\partial \rho/\partial x - 1/c^2 \cdot \partial p/\partial x\right) \\ u\, \partial v/\partial x \\ u\, \partial w/\partial x \\ (u+c)/2 \cdot (\partial p/\partial x + \rho c\, \partial u/\partial x) \\ u\, \partial Y_i/\partial x \end{bmatrix}. \tag{2}$$

In the above, $L_k^{(x)}$ are the wave amplitudes of the characteristic variables in x-direction, subscript t represents tangential (y and z) directions, $\mathbf{v}$ is the velocity vector, $c = \sqrt{\gamma RT}$ is the speed of sound, and

d_k and s_k are viscous and source terms corresponding to variable *k*. The main issue of the boundary treatment is to determine $L_k^{(x)}$'s for the incoming characteristic waves. Since the RHS of (2) cannot be computed in this case, proper approximations are needed as discussed in the following.

2.1. Conventional LODI relations

The original formulation of the characteristic boundary conditions for multi-dimensional Euler equations was done by Thompson [6,7], which has been extended to the Navier-Stokes equations [8-10], now commonly referred to as the Navier-Stokes characteristic boundary conditions (NSCBC). In these studies, the locally one dimensional inviscid (LODI) approximation was introduced to simplify the characteristic wave treatment at the boundary. For cases in which transverse, viscous and source terms are negligible, the LODI assumption is valid and the nonreflecting outflow boundary condition at $x = l_x$ is given by:

$$L_1^{(x)} = \alpha\left(p - p_\infty\right) + L_{1,\text{exact}}^{(x)} = \sigma c \frac{\left(1 - M^2\right)}{2l_x}\left(p - p_\infty\right) + L_{1,\text{exact}}^{(x)}, \tag{3}$$

where l_x is the domain length in the *x*-direction, p_∞ is the target pressure, *M* is the maximum Mach number along the boundary, and σ, the relaxation factor for pressure, is set to 0.25 [8]. $L_{1,\text{exact}}^{(x)}$ is the steady value of $L_1^{(x)}$ and is determined by the flow configuration [8,13,14].

Substituting (3) into (1), the temporal form of the nonreflecting boundary condition (referred to as the effective boundary condition) is obtained as [13,14]:

$$\frac{1}{2}\left(\frac{\partial p}{\partial t} - \rho c \frac{\partial u}{\partial t}\right) = -\alpha\left(p - p_\infty\right) + \left(\Im_1^{(x)} + V_1^{(x)} + S_1^{(x)} - L_{1,\text{exact}}^{(x)}\right), \tag{4}$$

where $\Im$, *V*, and *S* represent, respectively, the transverse, viscous, and source terms given by:

$$\begin{cases} \Im_1^{(x)} = -\left(\mathbf{v}_t \cdot \nabla_t p + \gamma p \nabla_t \cdot \mathbf{v}_t - \rho c \mathbf{v}_t \nabla_t u\right)/2, \\ V_1^{(x)} = \left(d_p - \rho c d_u\right)/2, \\ S_1^{(x)} = \left(s_p - \rho c s_u\right)/2. \end{cases} \tag{5}$$

Equation (4) shows the asymptotic steady behavior of the boundary pressure, *p*, with respect to its desired target value, p_∞. If any of the transverse, viscous, and/or source terms becomes large, the boundary pressure may drift from the target value significantly, which can also cause a numerical instability. Therefore, the conventional LODI approach is found to be valid only for inviscid, nonreacting, and unidirectional mean flows. Several previous studies have recognized the importance to consider the extra terms appearing in (4). For example, Sutherland and Kennedy [12] included the reaction source terms to allow a flame to pass through boundaries. These efforts, however, were done as a case-by-case refinement, and thus failed to provide a comprehensive resolution of all the anomalies observed in the reacting flow simulations. Equation (4) clearly shows that all relevant terms must be accounted for.

2.2. Improved characteristic boundary conditions

Based on the above consideration, a modified expression for the approximation for the incoming wave amplitude is now given by:

$$L_1^{(x)} = \alpha\left(p - p_\infty\right) + a\Im_{1,\text{exact}}^{(x)} + \left(1 - a\right)\Im_1^{(x)} + V_1^{(x)} + S_1^{(x)}, \tag{6}$$

such that the effective boundary condition becomes

$$\frac{1}{2}\left(\frac{\partial p}{\partial t} - \rho c \frac{\partial u}{\partial t}\right) = -\alpha\left(p - p_\infty\right) + a\left(\Im_1^{(x)} - \Im_{1,\text{exact}}^{(x)}\right), \tag{7}$$

where $\mathfrak{I}_{1,\text{exact}}^{(x)}$ is the steady target value of $\mathfrak{I}_1^{(x)}$, in analogy with p_∞ being the target value for pressure. The introduction of an additional damping term with coefficient a was found necessary in order to ensure numerical stability [13,14].

The modified characteristic boundary conditions are implemented in a three-dimensional DNS code [1]. Eighth-order explicit finite-difference scheme is used for special derivatives and a six-stage, fourth-order Runge-Kutta method is used for time integration with a PID error controller [17]. Since the body forces such as gravity are not considered in this study, the source terms in the momentum equations of (1) become zero or $s_u = s_v = s_w = 0$.

2.3. Vortex-convection test

As a first test problem, we adopt a single vortex convected by a uniform mean flow in the x-direction. Even in this simple configuration, the conventional NSCBC with LODI approximation revealed spurious pressure wave being generated as a strong vortical velocity field passes through the boundary. Equation (4) suggests that this is because the transverse convection terms are no longer negligible and must be properly accounted for.

From the asymptotic scaling based on the low Mach number expansion [18], the transverse damping coefficient, a, is found to be equal to the Mach number of the base flow: $a = M = u_\infty / c$. Following the test configuration in [8], the imposed vortex field is given by:

$$\begin{pmatrix} u \\ v \end{pmatrix} = \begin{pmatrix} u_\infty \\ 0 \end{pmatrix} + 1/\rho \begin{pmatrix} \dfrac{\partial \psi}{\partial y} \\ -\dfrac{\partial \psi}{\partial x} \end{pmatrix}, \quad \psi = C\exp\left(-\frac{(x-x_0)^2 + (y-y_0)^2}{2R_c^2} \right), \tag{8}$$

with the following flow conditions:

$$M = u_\infty / c = 0.05, \quad R_c / l_x = 0.1, \quad C/(cl_x) = -0.0025 .$$

The domain size is 2.0 mm × 2.0 mm with 200 grid points in each direction. An air stream is chosen at a reference condition of temperature and pressure at 300 K and 1 atm, respectively. The maximum velocity induced by the vortex is approximately at 5.26 m/s. The nonreflecting inflow boundary conditions [13,14] are adopted at $x = 0$ to suppress acoustic wave reflection at the inflow boundary. For the x-directional outflow boundary at $x = l_x$, three different boundary conditions are considered.

- BC1 is the conventional LODI approach as Poinsot and Lele proposed [8], with $L_{1,\text{exact}}^{(x)} = 0$, such that the effective boundary condition becomes:

$$\frac{\partial p}{\partial t} - \rho c \frac{\partial u}{\partial t} = -2\alpha(p - p_\infty) + 2\left(\mathfrak{I}_1^{(x)} + V_1^{(x)} + S_1^{(x)}\right). \tag{9}$$

- BC2 includes all the transverse and viscous terms in $L_1^{(x)}$, yielding the effective boundary condition with only the pressure damping term in RHS:

$$\frac{\partial p}{\partial t} - \rho c \frac{\partial u}{\partial t} = -2\alpha(p - p_\infty). \tag{10}$$

- BC3 is (7) with the transverse damping parameter $a = M = 0.05$ and $\mathfrak{I}_{1,\text{exact}}^{(x)} = 0$. The effective boundary condition or (7) becomes

$$\frac{\partial p}{\partial t} - \rho c \frac{\partial u}{\partial t} = -2\alpha(p - p_\infty) - 2M\mathfrak{I}_1^{(x)}, \tag{11}$$

Figure 1 shows the temporal variations of L2-norm of pressure difference throughout the simulations for the three boundary conditions tested. It is clearly seen that the L2-norm of Case BC3 continuously decreases, which implies that the vortex passes through the outflow boundary with much less disturbance compared to Cases BC1 and BC2.

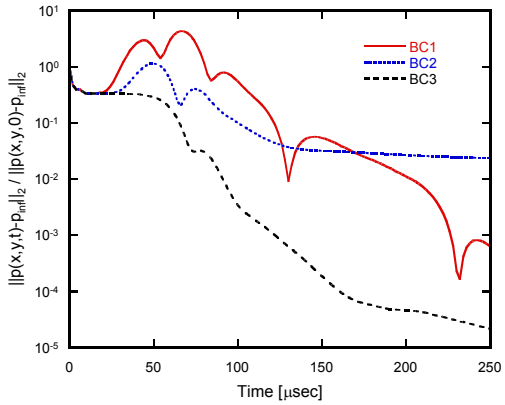

Figure 1. Temporal variations of L2-norm of pressure difference for Cases BC1-BC3.

The improved boundary conditions have also been tested in many other flow configurations [13,14], such as a laminar and turbulent counterflow diffusion flames, a temperature-induced ignition of homogeneous reactant mixtures, and a Poiseuille flow between two parallel plates; all the test simulations demonstrated that the modified characteristic boundary conditions reproduce accurate and robust solutions [14].

3. Soot and radiation models

As a new science model development, we have also implemented advanced soot and radiation models in the DNS code. High-fidelity modeling of thermal radiation is a challenging task since general consideration of radiation heat transfer involving many species and particles requires detailed knowledge of the absorption, emission, and scattering characteristics of each species that need to be integrated throughout the physical and wave number spaces. Although rigorous theory has been relatively well established and the radiative transfer equation (RTE) has been formulated [19,20], implementation of all the complex information into DNS is still cost-prohibitive, even at the level of terascale simulations. Therefore, some engineering approximations have to be made in order to compute the radiation heat flux terms at reasonable cost and time.

To account for the radiative heat transfer, the conservation equation for energy solved in S3D is written as:

$$\frac{\partial}{\partial t}(\rho e_t)+\nabla\cdot[(\rho e_t+p)\mathbf{v}]=\nabla\cdot(\boldsymbol{\tau}:\mathbf{v})+\nabla\cdot(\lambda\nabla T)-\nabla\cdot\left(\rho\sum_{i=1}^{N}h_iY_i\mathbf{V}_i\right)-\nabla\cdot\mathbf{q}_{\text{rad}}, \tag{12}$$

where the total specific energy is defined as

$$e_t=\frac{u^2+v^2+w^2}{2}+\sum_{i=1}^{N}h_iY_i-\frac{p}{\rho}. \tag{13}$$

In (12), $-\nabla\cdot\mathbf{q}_{\text{rad}}$ is the radiative heat transfer term which needs to be modeled. If all the gases are assumed gray (the absorption coefficients are independent of the wavelength), this term is expressed as:

$$-\nabla\cdot\mathbf{q}_{\text{rad}}=\kappa\left[\int_{4\pi}I(r,S)dS-4\pi I_b\right], \tag{14}$$

where κ is the absorption coefficient, $I(r,S)$ is the directional radiation intensity at a distance r and solid angle S, and I_b is the blackbody radiation intensity. In the present study, two radiation models are tested for their relative accuracy and computational efficiency. First, the optically thin radiation model (OTM) is one of the simplest methods for calculating radiation. If the gases are optically thin, the integral term in (14) vanishes such that the radiative heat transfer term is simplified to an explicit expression:

$$-\nabla\cdot\mathbf{q}_{\mathrm{rad}}=-4\sigma\kappa\left(T^4-T_\infty^4\right). \tag{15}$$

This model will serve as a baseline study case, whose accuracy is expected to degrade as the gas medium in the reacting flows becomes more radiatively active. If the gases are optically thick, a more comprehensive treatment of radiative transfer equations (RTE) is needed to determine the radiation intensity. For this purpose, the discrete ordinate method (DOM), first proposed by Chandrasekhar [21], has been widely accepted as an optimal choice in favor of its reasonable accuracy and cost-effectiveness.

The RTE for DOM is represented by a set of equations for an intensity that is angularly averaged over each of a finite number of ordinate directions. Integrals over a range of solid angles are approximated by a weighted sum of the angular quantities [19]. Thus, the discrete equations of transfer are given by:

$$\alpha_m\frac{\partial I_m}{\partial x}+\delta_m\frac{\partial I_m}{\partial y}+\gamma_m\frac{\partial I_m}{\partial z}=\kappa(S)I_b(S)-\left(\kappa(S)+\sigma_s(S)\right)I_m(S)+\frac{\sigma_s(S)}{4\pi}\sum_{m'}w_{m'}I_{m'}(S)\Phi_{m'm}(S). \tag{16}$$

By solving the finite number of equations for the intensity by iteration, the radiation intensity and heat loss at every location and time can be found.

The soot formation processes are described using a semi-empirical model developed by Moss et al. [22,23]. To describe the soot dynamics, in addition to the Navier-Stokes equations for multi-component reacting flow, the transport equations of soot number density and soot mass fraction are solved, which are given in normalized form by:

$$\begin{cases}\dfrac{\partial}{\partial t}\left(\dfrac{n_{\mathrm{s}}}{N_0}\right)+\dfrac{\partial}{\partial x_j}\left(\dfrac{n_{\mathrm{s}}}{N_0}u_j\right)=\dfrac{1}{\mathrm{Re}_a}\dfrac{\partial}{\partial x_j}\left[\dfrac{\nu}{\mathrm{Sc}_{\mathrm{s}}}\dfrac{\partial}{\partial x_j}\left(\dfrac{n_{\mathrm{s}}}{N_0}\right)\right]-\dfrac{\partial}{\partial x_j}\left(V_{t,j}\dfrac{n_{\mathrm{s}}}{N_0}\right)+\dot{\omega}_{(n_{\mathrm{s}}/N_0)},\\ \dfrac{\partial}{\partial t}\left(\rho Y_{\mathrm{s}}\right)+\dfrac{\partial}{\partial x_j}\left(\rho Y_{\mathrm{s}}u_j\right)=\dfrac{1}{\mathrm{Re}_a}\dfrac{\partial}{\partial x_j}\left(\dfrac{\nu}{\rho\mathrm{Sc}_{\mathrm{s}}}\dfrac{\partial Y_{\mathrm{s}}}{\partial x_j}\right)-\dfrac{\partial}{\partial x_j}\left(\rho Y_{\mathrm{s}}V_{t,j}\right)+\dot{\omega}_{(\rho Y_{\mathrm{s}})},\end{cases} \tag{17}$$

where n_{s} is soot number density, Y_{s} is soot mass fraction, N_0 is the Avogadro number, and $V_{t,j}$ is the thermophoresis velocity of a soot particle given by [26]:

$$V_{t,j}=-0.54(1/T)\partial T/\partial x_j\ .$$

The soot formulation rates in (17) are given by:

$$\begin{cases}\dot{\omega}_{(n_{\mathrm{s}}/N_0)}=c_\alpha\rho^2T^{1/2}X_{\mathrm{F}}\exp(-T_\alpha/T)-c_\beta T^{1/2}(n_{\mathrm{s}}/N_0)^2,\\ \dot{\omega}_{(\rho Y_{\mathrm{s}})}=c_\gamma\rho T^{1/2}X_{\mathrm{F}}\exp(-T_\gamma/T)n+c_\delta c_\alpha\rho^2T^{1/2}X_{\mathrm{F}}\exp(-T_\alpha/T)-\dot{\omega}_{\mathrm{ox}}S,\\ \dot{\omega}_{\mathrm{ox}}=1.085\times10^5X_{\mathrm{O}}T^{-1/2}\exp(-19778/T).\end{cases} \tag{18}$$

where X_{F} is the mole fraction of fuel (C_2H_4), X_{O} is the mole fraction of oxidizer (O_2), and S is the surface area per unit volume [1/m] given by $S=\pi d^2n_{\mathrm{s}}=(36\pi n_{\mathrm{s}})^{1/3}f_v^{2/3}$. The parameters used in this study are given by $c_\alpha=6\times10^6$, $c_\beta=2\times10^{14}$, $c_\gamma=0.8\times10^{-14}$, $c_\delta=144$, $T_\alpha=4.61\times10^4$, and $T_\gamma=1.26\times10^4$. For soot radiation, the absorption coefficient of soot is defined by $\kappa_s=1118f_vT$ [1/m].

4. Flame-vortex interaction

One of the goals of the present study is to understand the fundamental characteristics of interaction between turbulence and chemistry in the presence of soot and radiation. As a model problem, we first study the interaction of counter-rotating vortices and laminar nonpremixed flame, which represents a canonical configuration as an elementary subset of more complex turbulent combustion phenomena. To avoid excessive complication of the problem, a one-step ethylene-air reaction with the semi-empirical soot model shown in (17) was used.

4.1. Transient dynamics of soot

The left-most images in Fig. 2 show the initial condition of the simulation. The domain size is 2.48cm × 2.48cm with a grid resolution of 400 × 400. A steady laminar diffusion flame is first established in

an opposed flow (inflow at the left and right boundaries), and two pairs of counter-rotating vortices (shown in black line contours) are superimposed. The inlet velocities of both fuel and air sides are equal to 0.78m/s and overall strain rate is approximately 63s^{-1}. The vortex pairs are subsequently convected onto the flame by the mean flow as well as self-induced drift, thereby penetrating through the flame with vigorous interaction until the vortices pass through the outflow boundaries. A single vortex is given by [25,26]:

$$\frac{u_\theta(r)}{u_{\theta,\max}} = \frac{C\sigma^2}{2\pi r^2[1-e^{-(r/\sigma)^3}]}, \tag{19}$$

where C = 9.883 and σ is the effective radius of the vortex such that the maximum azimuthal velocity, $u_{\theta,\max}$ occurs at $r = 0.9\sigma$. σ = 0.3cm and $u_{\theta,\max}$ = 3m/s are chosen for the test.

Figure 2 shows the temporal variations of (a) temperature and vorticity and (b) soot volume fraction at t = 0, 3, 5, and 20 msec. DOM was used as radiation solver. As the vortices are convected to the flame, the soot quenching occurs at the center part of the flame (at t = 3 msec) even the flame is not completely extinguished. As vortices pass through the boundaries, both the highly stretched flame and the soot layer gradually recover the original steady solution.

Figure 3 shows temporal variations of the local maximum soot volume fraction, f_v, and soot number density, n_s. Comparing Figs. 2 and 3, it is recognized that the maximum n_s depends strongly on the maximum temperature. The instantaneous burst in peak temperature zones toward the fuel side of the flame results in a rise in the production of soot particles (at t = 3 msec). On the other hand, the maximum soot volume fraction does not follow the number density but is rather closely related to the soot oxidation process. In other words, the maximum f_v appears in low temperature region where the soot oxidation process is turned off at t = 5 msec. After the vortices effectively carry the soot particles out of a high temperature region into a low temperature region, the soot oxidation rate is reduced and there is sufficient residence time to increase the soot volume fraction. Consequently, the maximum soot volume fraction is observed in the low temperature region, as seen in figure 2 at t = 5 msec.

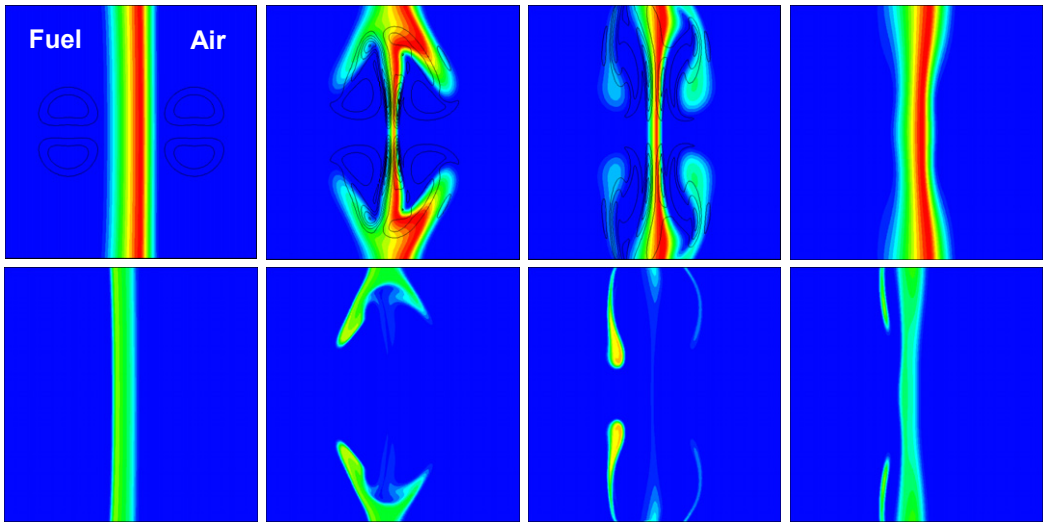

Figure 2. Temporal variations of temperature (flood) and vorticity (black lines) (top) and s oot volume fraction, f_v, (bottom) with the optically thin radiation model. From left to right, t = 0, 3, 5, and 20 msec.

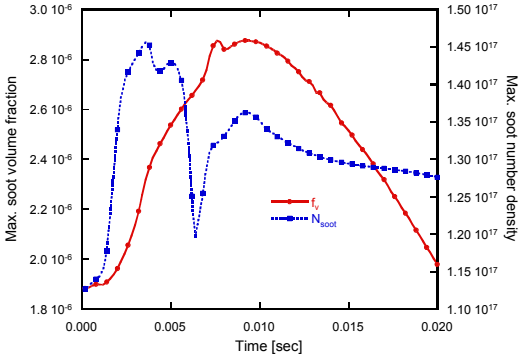

Figure 3. Temporal variations of the local maximum soot volume fraction, f_v and soot number density, n_s.

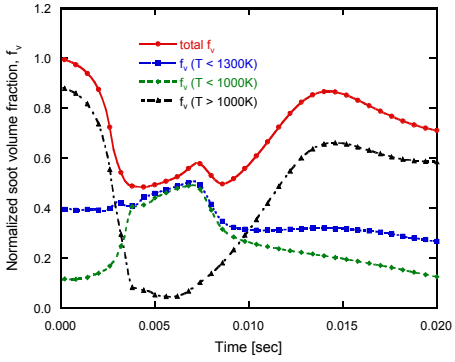

Figure 4. Temporal variations of the integ rated soot volume fraction.

Consistent behavior is also found in the volume-integrated soot volume fraction. Figure 4 shows temporal variations of the volume-integrated f_v in different temperature regions. For example, "f_v (T < 1000K)" represents the total soot volume fraction in the region at which temperature is less than 1000 K. Even if soot extinction occurs during t = 3 and 5 msec in figure 1, f_v (T < 1000K) is increased during that period, which implies that soot is pushed toward the low temperature region by vortices and grows into a larger volume.

Finally, figure 5 shows the temporal variations of the flame volume. The flame volume is defined such that $V_{flame}(T > 2000K)$ represents the total volume within the domain that is at temperatures above 2000K. Also overlaid is the volume-integrated soot number density. The results clearly show that the total soot number density correlates strongly on the volume of high temperature region, primarily due to the fact that the maximum soot number density occurs at the maximum temperature.

4.2. Radiation models

To assess the solution accuracy depending on the complexity of the model, two different radiation models (OTM and DOM) are tested against each other, under the same conditions used in section 4.1. Figure 6 shows the temporal variations of total radiative heat loss with OTM and DOM. While the agreement between the two models appears to be very good at near steady conditions, the discrepancy becomes significant during the rapid transition period of the strong flame-vortex interaction. In

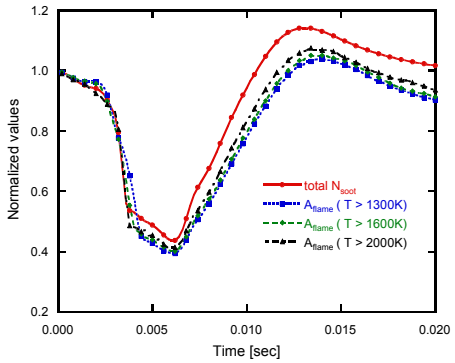

Figure 5. Temporal variations of the integrated soot number density and flame volume.

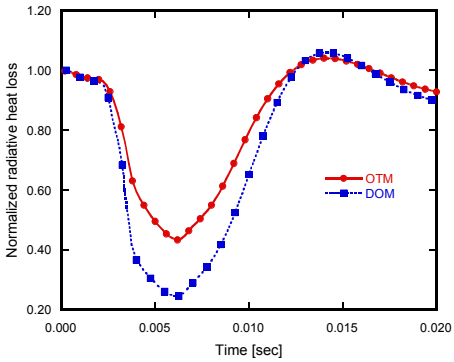

Figure 6. Temporal variations of total radiative heat loss in OTM and DOM

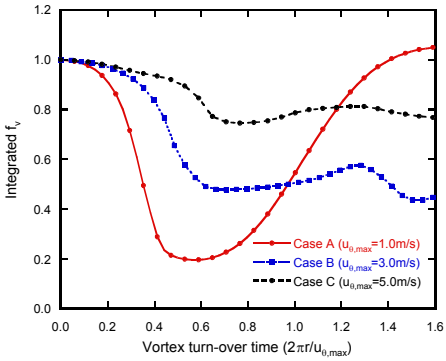

Figure 7. Temporal variations of the integrated soot volume fraction for Cases A-C.

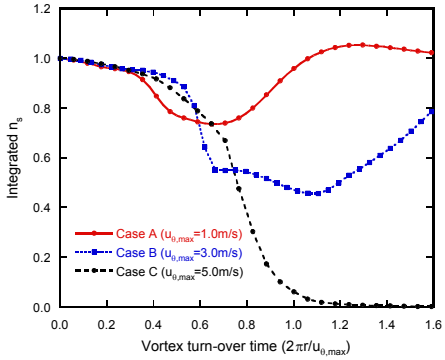

Figure 8. Temporal variations of the integrated soot number density for Cases A-C.

particular, during the soot extinction period (t = 3 and 5 msec in figure 2), OTM is found to overestimate the radiative heat loss compared to DOM, by up to a factor of two. This demonstrates the importance of the advanced radiation models in high-fidelity simulations.

4.3. Effects of the vortex strength

To further examine the importance of the time scales of the unsteady flow relative to those of soot formation, three different vortex strength cases were simulated. Case A has the weakest vortex strength with $u_{\theta_{\max}}$ = 1m/s, Case B has a medium strength with $u_{\theta,\max}$ = 3m/s, which corresponds to the case in section 4.1, and Case C is the strongest vortex with $u_{\theta,\max}$ = 5m/s, leading to a complete soot and flame extinction during the interaction.

Figure 7 shows the temporal variations of integrated soot volume fraction for Cases A-C. For Case A, even if the vortex strength is the weakest among the three cases, the total volume fraction in the domain is reduced most significantly at the early stage of flame-vortex interaction. On the other hand, the strongest vortex case (Case C) yields only a small amount of reduction in the total soot volume fraction. This is interpreted from the fact that, as the vortex strength increases, more soot particles are convected from the high temperature region into the low temperature, fuel-rich region, as observed in Fig. 2. The soot particles left in the fuel-rich regions are allowed to grow at a faster rate. Consequently, Case C shows a higher overall soot volume fraction despite the partial extinction of the flame and soot layers.

Figure 8 shows the temporal variations of integrated soot number density for Cases A-C. Comparison of Figs. 7 and 8 confirms that a substantial fraction of the soot volume fraction increase in Case C is by the surface growth in the fuel-rich region rather than by the generation of new soot particles in the flame which is turned off due to flame extinction. For Case A, even if the total volume fraction is reduced by the vortex-induced strain during the early stage of the flame-vortex interaction, it recovers the steady value at the end because the weak vortices do not extinguish the flame so that the soot generation in the flame can also recover easily.

The above results demonstrate that the flame-soot-radiation interaction in highly turbulent combustion can be far more complex than a simple steady description can predict. The high-fidelity simulations provide detailed information of the complex soot dynamics that provides insights toward improved submodels in larger-scale simulations.

5. Conclusions

Some recent advances in the development of high-fidelity direction simulations of turbulent reacting flows have been presented. First, improved characteristic boundary conditions were developed based on the observation that the transverse, viscous, and source terms must be properly accounted for in the approximations of the incoming wave amplitudes. Appropriate transverse damping parameters were

identified based on the asymptotic scaling in terms of the flow Mach number. Through a variety of test simulations, it was demonstrated that the new boundary conditions can reproduce more accurate steady and transient solutions with improved numerical stability.

We have also successfully developed and integrated advanced radiation and soot models into the direct simulation code, in order to study fundamental issues of soot-radiation-turbulence interactions occurring in nonpremixed combustion. The new physical models allow representation of sooting/radiating nonpremixed flames with substantially improved realism. The detailed simulation data provide accurate information about the local and instantaneous soot behavior and the effects of the neighboring conditions. The generated numerical databases will prove valuable in developing more physically-based soot formation submodels in device-level simulations based on RANS or LES.

Acknowledgments
This work was supported by the Department of Energy, Office of Basic Energy Science, SciDAC Computational Chemistry Program.

References

[1] H.G. Im, A. Trouvé, C.J. Rutland, and J.H. Chen 2005 Terascale high-fidelity simulations of turbulent combustion with detailed chemistry, http://www.purl.org/net/tstc.
[2] E. Engquist and A. Majda 1977 *Math. Comput.* **31** 629
[3] G.W. Hedstrom 1979 *J. Comput. Phys.* **30** 222
[4] D.H. Ruddy and J.C. Strikwerda 1980 *J. Comput. Phys.* **36** 55
[5] D.H. Ruddy and J.C. Strikwerda 1981 *Comput. Fluids.* **9** 327
[6] K.W. Thompson 1987 *J. Comput. Phys.* **68** 1
[7] K.W. Thompson 1990 *J. Comput. Phys.* **89** 439
[8] T.J. Poinsot and S.K. Lele 1992 *J. Comput. Phys.* **101** 104
[9] M. Baum, T.J. Poinsot, and D. Thévenin 1994 *J. Comput. Phys.* **176** 247
[10] N. Okong'o and J. Bellan 1994 *J. Comput. Phys.* **176** 330
[11] T.J. Poinsot and D. Veynante 2001 *Theoretical and Numerical Combustion* (Philadelphia: R.T. Edwards Inc)
[12] J.C. Sutherland and C.A. Kennedy 2003 *J. Comput. Phys.* **191** 502
[13] C.S. Yoo, Y. Wang, A. Trouvé, and H.G. Im 2005 Characteristic boundary conditions for direct numerical simulations of turbulent counterflow flames, *Combust. Theory Modelling*, in press.
[14] C.S. Yoo and H.G. Im 2005 Improved characteristic boundary conditions for direct numerical simulations with multi-dimensional, viscous, and reaction effects, in preparation.
[15] C.R. Kaplan, C.R. Shaddix and K.C. Smyth 1996 *Combust. Flame* **106** 392
[16] F. Lin, H. Guo and G.J. Smallwood 2004 *Combust. Flame* **138** 136
[17] C.A. Kennedy, M.H. Carpenter, and R.H. Lewis 2000 *Appl. Num. Math.* **35** 177
[18] B. Müller 1999 Low mach number asymptotics of the Navier-Stokes equations and numerical implications, von Karman Institute for Fluid Dynamics Lecture Series 1999-03, 30th computational fluid dynamics
[19] M.F. Modest 1993 *Radiative Heat Transfer* (New York; McGraw-Hill)
[20] R. Siegel and J. Howell 2002 *Thermal Radiation Heat Transfer 4th ed.* (New York; Taylor and Francis)
[21] S. Chandrasekhar 1960 *Radiative Transfer* (New York; Dover)
[22] J.B. Moss, C.D. Stewart, and K.J. Young 1995 *Combust. Flame* **101** 491
[23] J.B. Moss, C.D. Stewart, and K.J. Syed 1988 *Proc. Combust. Inst.* **22** 413
[24] S.K. Friedlander 2000 *Smoke Dust and Haze: Fundamentals of Aerosol Dynamics* 2nd ed. (New York; Oxford University Press)
[25] H.G. Im and J.H. Chen 1999 *Combust. Flame* **119**, 436
[26] C.S. Yoo and H.G. Im 2005 *Proc. Combust. Inst.* **30**, 349